Acta Materialia 320 (2026) 122715

Contents lists available at ScienceDirect

Acta Materialia

journal homepage: www.elsevier.com/locate/actamat

Full length article

Simultaneous control of phase stability and crystallographic texture for low-modulus biomedical β-type Ti–Cr–Al alloys by in-situ-alloying LPBF

Takuya Ishimoto [a,b], Soki Hoshino [a], Yuki Nishikawa [a], Masakazu Tane [a,c], Kazuhisa Sato [d,e], Hyoung Seop Kim [f], Takayoshi Nakano [a,c,*]

[a] Division of Materials and Manufacturing Science, Graduate School of Engineering, The University of Osaka, 2-1, Yamadaoka, Osaka, Suita, 565-0871, Japan
[b] Titanium Research Center (TRC), University of Toyama, 3190, Gofuku, Toyama, Toyama, 930-8555, Japan
[c] 3DPTec Integrated Center, The University of Osaka, 2-1, Yamadaoka, Osaka, Suita, 565-0871, Japan
[d] Research Center for Ultra-High Voltage Electron Microscopy, The University of Osaka, 7-1, Mihogaoka, Osaka, Ibaraki, 567-0047, Japan
[e] Faculty of Engineering, Kyushu University, 744 Motooka, Nishi-ku, Fukuoka, Fukuoka, 819-0395, Japan
[f] Graduate Institute of Ferrous & Eco Materials Technology, Pohang University of Science and Technology (POSTECH), Pohang, 37673, South Korea

ARTICLE INFO

Keywords:
β-Ti alloy
In situ alloying
Laser powder bed fusion
Phase stability
Crystallographic texture
Young's modulus

ABSTRACT

Laser powder bed fusion (LPBF) offers not only geometric freedom, but also a unique route to co-design composition-based phase stability and crystallographic texture, which are critical for realizing low-modulus Ti alloys. In this study, we fabricated Ti–Cr and Ti–Cr–Al alloys by the in situ alloying of elemental powders and programmed single-crystal-like textures (⟨100⟩, ⟨110⟩, or ⟨111⟩ // build direction (BD)) via tailored scanning strategies. By employing processing conditions that yielded a melt pool depth far greater than the layer thickness, compositionally uniform builds were achieved through multiple remelting events. In Ti–12Cr (wt.%), which has relatively low β-phase stability, the ω phase was observed despite not being detected in its solution-treated-and-quenched counterpart. This observation suggests that the LPBF-specific thermo-mechanical history, including a tensile residual stress of 353 MPa, may have contributed to ω-phase formation. The addition of Al suppressed the formation of ω, resulting in a single-phase β matrix. Furthermore, scan-strategy-dependent textures were consistently observed across all the compositions. The elastic modulus showed pronounced orientation-dependent anisotropy, reaching ~60 GPa along ⟨100⟩ in a Ti–12Cr–3Al composition, whereas the BD-parallel yield strength approached 800–1000 MPa depending on the texture, producing elastic admissible strains that surpass those of reported LPBF-fabricated Ti–6Al–4V. Based on these findings, we propose an additive manufacturing process-aware design framework in which alloy composition, LPBF-specific thermo-mechanical history, and crystallographic texture contribute collectively to phase stability and directional mechanical properties in metastable β-Ti alloys.

1. Introduction

Laser powder bed fusion (LPBF), a type of additive manufacturing (AM), offers high-resolution geometric control by selectively melting fine metal powders layer-by-layer. This technique has been widely adopted to produce patient-specific implants because it can precisely fabricate complex geometries that conform to anatomical data [1,2]. Importantly, LPBF also provides opportunities for compositional and microstructural control, which are particularly relevant for materials such as Ti-based alloys, where composition-sensitive metastable phases can be intentionally utilized to tailor mechanical properties.

Ti alloys are widely used in biomedical and structural applications owing to their excellent biocompatibility, corrosion resistance, and high strength-to-weight ratios. Among their unique features, the ability to tailor phase stability and crystallographic texture is pivotal for tuning their mechanical performance, particularly their elastic modulus, to meet application-specific demands. The phase composition of Ti alloys is susceptible to their composition [3,4]. The stability of the metastable β phase, for instance, is strongly influenced by the type, amount, and combination of β-stabilizing elements, such as Cr, Mo, Nb, or V. When

* Corresponding author at: Division of Materials and Manufacturing Science, Graduate School of Engineering, The University of Osaka, 2-1, Yamadaoka, Osaka, Suita, 565-0871, Japan.
E-mail address: nakano@mat.eng.osaka-u.ac.jp (T. Nakano).

https://doi.org/10.1016/j.actamat.2026.122715
Received 18 May 2026; Received in revised form 31 July 2026; Accepted 30 August 2026
Available online 31 August 2026

the alloy composition is finely tuned to remain within the single-phase metastable β field, the resulting microstructure exhibits pronounced elastic anisotropy, enabling a reduction in Young's modulus along the ⟨100⟩ direction owing to the intrinsic crystallographic behavior of the body-centered cubic structure [5,6]. This low-modulus characteristic is particularly desirable for orthopedic implants to mitigate stress shielding [7].

However, the formation of high-stiffness secondary phases, such as the α (or α′) and ω phases, within the metastable β matrix can significantly increase the elastic modulus, thereby compromising the functional target [7]. Because the formation of these phases is compositionally driven, precise control of the alloy composition is essential to retain the desired low-modulus metastable β phase. In conventional approaches, exploring various compositions typically requires the preparation of multiple pre-alloyed powders, which is time-consuming and costly. Therefore, a more flexible and efficient strategy is to enable direct compositional tuning during the manufacturing process, for example, by blending elemental powders and alloying them in situ [8–11]. This approach can significantly accelerate the screening and optimization of composition-sensitive Ti alloys.

Beyond compositional control in LPBF, crystallographic texture can be tailored by manipulating the scanning strategy, laser beam profile, melt pool geometry, and local solidification conditions [12–16]. Studies on biomedical β-Ti alloys have demonstrated that the development of strong ⟨100⟩-oriented textures can markedly reduce Young's modulus along the oriented direction. By adjusting processing parameters, LPBF can produce a wide range of texture states, from near-random orientations to highly aligned single-crystal-like textures [17], providing an effective strategy for regulating mechanical anisotropy [18,19]. In particular, matching the layer-wise scanning strategy with the rotational symmetry of cubic alloys enables the selective formation of preferred ⟨100⟩, ⟨110⟩, or ⟨111⟩ orientations along the build direction (BD) [20].

This simultaneous control of shape and crystallographic texture opens up new possibilities in product design [20], where not only the external form but also the internal functional properties can be spatially optimized. In this context, texture programming within a single component enables the site-specific tailoring of mechanical properties, elevating LPBF from a geometric-shaping tool to a platform for advanced functionally graded materials. This approach is considered a promising avenue for the next generation of topology–material co-optimized structures with potential applications in biomedical and lightweight structural devices [20].

To exploit this concept fully, it is essential to integrate the geometric and texture-control capabilities of LPBF with precise compositional design, especially in systems such as Ti-based alloys, where mechanical properties are susceptible to subtle changes in phase stability. In this study, we explored an in situ alloying approach using LPBF, in which elemental powders are blended and alloyed during the printing process, bypassing the need for pre-alloyed powder fabrication and enabling flexible composition tuning.

Specifically, we focused on the Ti–Cr binary and Ti–Cr–Al ternary systems to examine the evolution of phase stability, microstructure, crystallographic texture, and mechanical properties as a function of composition. The Ti–Cr system is particularly suitable for studying composition-sensitive phase stability and designing low-modulus β-Ti alloys for several reasons. First, Cr exhibits a high β-stabilizing coefficient of 1.6 in the Mo-equivalent (Mo_{eq}) calculation [21], making it one of the most effective β stabilizers in Ti alloys [22]; consequently, even small variations in Cr concentration can sensitively alter the phase stability of the alloy. Second, the melting point of Cr is relatively close to that of Ti, which is advantageous for reducing residual unmelted powder and associated compositional deviations during in situ alloying by LPBF. Third, the relatively narrow solid–liquid two-phase region of Ti–Cr alloys is also expected to suppress solidification-induced microsegregation and promote chemical homogenization during repeated melting and remelting events involved in LPBF. Additionally, composition-dependent phase stability and Young's modulus have been reported in conventionally processed Ti–Cr alloys, including the β-metastable composition region [22], providing a foundation for clarifying the LPBF-specific effects on composition–phase–property relationships.

Al was further introduced as a minor alloying element to suppress ω-phase formation and adjust the phase stability of the metastable β matrix [23]. Unlike Sn, which suppresses ω formation without substantially changing the electron-to-atom ratio (*e/a*) [24,25], Al decreases the *e/a* ratio while inhibiting ω formation. Therefore, the Ti–Cr–Al system enables investigation of the simultaneous ω-phase suppression and low-modulus β-phase stabilization through the combined effects of Cr and Al.

By integrating composition-based phase-stability control with LPBF-induced crystallographic texture engineering, this study aims to develop an AM process-aware design framework for low-modulus β-Ti alloys with tailorable functionality, in which phase constitution, elastic anisotropy, Young's modulus, yield strength, and elastic admissible strain can be deliberately tuned.

2. Experimental procedures

2.1. Alloy compositions

For the Ti–Cr binary system, compositions with *e/a* around 4.2 were chosen, where the formation of an unstable β phase is expected to yield a low Young's modulus [26]. It has been reported that Young's modulus exhibits a local minimum near an *e/a* of 4.2; below this range, the precipitation of ω or α″ phases leads to an increase in the modulus, whereas above it, stabilization of the β phase similarly raises the modulus. However, suppression of the ω and α″ phases enables the realization of even lower Young's moduli at *e/a* values below 4.2. As Al suppresses ω-phase formation, Ti–Cr–Al ternary alloys were also explored in addition to the Ti–Cr binary system. Nine alloy compositions were prepared, as summarized in Table 1.

2.2. LPBF fabrication of Ti–Cr and Ti–Cr–Al alloys via in situ alloying

Spherical pure Ti powder (Osaka Titanium Technologies, Japan), pure Cr powder (Advanced Engineering Materials, China), and pure Al powder (Toyo Aluminum, Japan) were weighed to obtain the alloy compositions listed in Table 1. The powders were mixed for >12 h by rotation and swinging in a tumbler (Aichi Electric, Japan) to achieve a uniform powder distribution. Energy-dispersive X–ray spectroscopy (EDS) images of the powders after mixing are presented in Supplementary Fig. S1.

Rectangular specimens with dimensions of 5 mm (depth) × 5 mm (length) × 25 mm (height) were prepared using an LPBF apparatus (EOS M 290; EOS, Germany). A Yb fiber laser was used with a laser power of 360 W, scanning speed of 1200 mm/s, scan pitch of 100 μm, and layer thickness of 60 μm. This combination of laser conditions was tuned to form strong single-crystal-like textures in β-Ti alloys [27]. Three different laser scanning strategies (SS), namely, ±X_SS, ±XY_SS, and +120°Rot_SS (Supplementary Fig. S2), were used to obtain single-crystal-like textures with three different crystallographic orientations: ⟨110⟩, ⟨100⟩, and ⟨111⟩, parallel to the BD [20]. LPBF was performed in an Ar gas atmosphere.

2.3. Compositional analyses

Chemical composition analyses were conducted to investigate the overall elemental composition of the samples. The concentrations of Cr and Al were analyzed using inductively coupled plasma (ICP; ICPS-8100, Shimadzu, Japan), whereas that of oxygen (O) was analyzed using an inert gas fusion method (TC-436AR, LECO, USA). Additionally,

Table 1
Nominal compositions of the prepared alloys, and the calculated Mo equivalent (Mo_{eq}) and electron-to-atom ratio (e/a).

Alloys (wt.%)	6Cr	12Cr	14Cr	16Cr	20Cr	12Cr-3Al	14Cr-3Al	16Cr-3Al	20Cr-3Al
Mo_{eq}	9.6	19.2	22.4	25.6	32.0	16.2	19.4	22.6	29.0
e/a	4.11	4.22	4.26	4.30	4.37	4.17	4.20	4.24	4.31

the compositional distribution was investigated using EDS (Aztec 3.1, Oxford Instruments, UK) equipped with a field-emission scanning electron microscope (FE-SEM) (JIB-4610F, JEOL, Japan).

2.4. Phase identification

The phase composition of the alloys was identified by X-ray diffraction (XRD; X'Pert PRO, PANalytical, Netherlands) with Cu Kα radiation at an accelerating voltage and current of 40 kV and 40 mA, respectively. Measurements were performed on the *xy*-plane of the specimen fabricated using ±XY_SS using a 2θ scan from 20° to 100° at a scan rate of 0.02° /s and a scan interval of 0.0167°.

2.5. Crystallographic texture analysis

The specimen cross-sections were polished with finely graded emery papers up to #4000 and mirror-polished using colloidal silica. To obtain information on the crystal orientation distribution, an electron backscatter diffraction (EBSD) system (NordlysMax^3; Oxford Instruments, Abingdon, UK) equipped on an FE-SEM was used. EBSD was performed at an accelerating voltage of 20 kV and a step size of 2 μm. Inverse pole figure (IPF) maps and pole figures were generated using AztecHKL 4.4 (Oxford Instruments).

2.6. Microstructural characterization

Microstructural characterization was performed by transmission electron microscopy (TEM; JEM-3010, JEOL) and scanning TEM (STEM; JEM-ARM-200F, JEOL). Foil samples for TEM observation were prepared using a twin-jet electropolishing machine (Tenupol-3, Struers, Denmark) with a solution of 65% methanol, 30% butanol, and 5% $HClO_4$ at approximately 263 K. TEM was operated at an accelerating voltage of 300 kV, and STEM at 200 kV.

2.7. Mechanical properties evaluation

Tensile specimens with a gauge length of 5 mm, width of 2 mm, and thickness of 0.8 mm were prepared. Tensile tests were conducted using an Instron-type testing machine (AGX-50kNV, Shimadzu) at room temperature at an initial strain rate of 1.67×10^{-4} s^{-1}. The tensile load was applied parallel to BD. To determine Young's modulus, a strain gauge (KFGS-2N-120-C1–11 L1M2R, Kyowa Electronic Instruments, Japan) was directly attached to the specimen surface parallel to the loading axis to monitor the deformation during loading. Young's modulus was calculated by linear least-squares fitting of the stress–strain curve measured over a stress range of 400–600 MPa. The coefficient of determination for all fittings exceeded 0.98. The tests were conducted in triplicate, and the averaged values were reported.

2.8. Residual stress evaluation

Residual stresses were evaluated using XRD. The diffractometer alignment and measurement procedures were performed in accordance with ASTM E915–10 [28]. Residual stress measurements were conducted on the XZ surface using the $\sin^2\psi$ side-inclination method, in which the specimen was tilted in a direction perpendicular to the diffraction plane. This configuration enabled evaluation of the normal component of residual stress along the *z*-axis, σ_z, on the XZ surface. In the $\sin^2\psi$ method, the diffraction peak position was plotted as a function of $\sin^2\psi$ and fitted by the least-squares method. The slope of the fitted line, $\Delta 2\theta/\Delta(\sin^2\psi)$, was used to determine the lattice strain, which was subsequently converted into residual stress, σ, using Young's modulus, E, and Poisson's ratio, ν, according to the following equation:

$$\sigma = -\frac{E}{2(1+\upsilon)} \cdot \cot\theta_0 \cdot \frac{\pi}{180} \cdot \frac{\Delta 2\theta}{\Delta\left(\sin^2\psi\right)}$$

where θ_0 is half of the diffraction angle for the stress-free state. The (211) diffraction peak at approximately $2\theta = 70.5°$ was used for the analysis, and measurements were performed at 11 ψ angles ranging from 0° to 45°. A Poisson's ratio of 0.33 was used in the calculation. Young's modulus was taken as the average of the values obtained from the tensile tests of the ⟨100⟩-, ⟨110⟩-, and ⟨111⟩-oriented 12Cr specimens, as presented in the Results section. The stress-free diffraction angle, θ_0, was determined using the specimen after stress-relief annealing.

2.9. Statistical analyses

Quantitative results are expressed as the mean ± standard deviation. One-way analysis of variance was performed to evaluate differences in Young's modulus across scanning strategies (i.e., preferential crystallographic orientations), and post-hoc Tukey's HSD tests were applied for multiple comparisons. Statistical significance was set at $p < 0.05$. SPSS version 25 software (IBM, Armonk, NY, USA) for Microsoft Windows was used for all statistical analyses.

3. Results

3.1. Composition and compositional distribution

Table 2 lists the composition of the alloys measured using ICP and inert-gas fusion. In all examined alloys, the measured concentrations of Cr and Al were lower than their respective nominal compositions. This was likely owing to the evaporation of Cr and Al during melting because their saturation vapor pressures at 2000 K are approximately two and three orders of magnitude higher than that of Ti, respectively [29]. The oxygen concentration was approximately 0.1%, which was similar to that of the ingots produced by arc melting. Fig. 1 shows the composition distribution map near the top surface and at the center of the product. Although compositional inhomogeneity was observed near the top surface, the interior of the product exhibited a homogeneous distribution of elements, and no evidence of residual unmelted powders or incomplete melting was detected.

3.2. Constituent phases, crystallographic texture, and microstructure

The XRD peak profiles are shown in Fig. 2. In the 6Cr alloy, diffraction peaks corresponding to both α′ and β phases were observed. Although the α′ and α phases share the same HCP crystal structure and are difficult to distinguish by XRD, the exceptionally high cooling rates inherent to the LPBF process typically lead to the formation of the α′ phase via a martensitic transformation. In contrast, for the alloys with higher Mo-equivalent and e/a values than 6Cr, only peaks associated with the β phase were detected. These β-phase peaks shifted progressively toward higher angles as the Cr content increased, indicating a reduction in lattice parameter owing to the smaller atomic radius of Cr

Table 2
Composition of each alloy.

Alloys (wt.%)	6Cr	12Cr	14Cr	16Cr	20Cr	12Cr-3Al	14Cr-3Al	16Cr-3Al	20Cr-3Al
Cr	5.4	11.9	13.2	15.1	19.3	11.6	13.0	14.8	19.9
Al	-	-	-	-	-	2.81	2.85	2.76	2.74
O	0.10	0.12	0.10	0.09	0.11	0.11	0.11	0.11	0.11

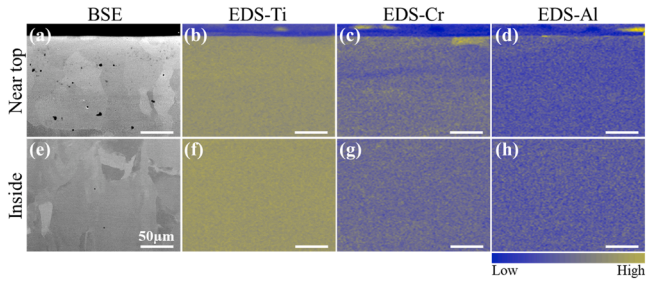

Fig. 1. (a–d) BSE and EDS mapping images of the top surface of the product; (e–h) corresponding images of the interior region. (a, e) BSE images; (b–d, f–h) EDS elemental maps. Although compositional inhomogeneity was observed at the top surface owing to insufficient mixing, a uniform elemental distribution was achieved in the interior.

relative to Ti.

Fig. 3 shows IPF maps of the β phase (colored according to the crystal orientation projected along the surface normal) obtained from three orthogonal planes, along with the corresponding pole figures. The application of the three distinct scanning strategies resulted in the formation of three different crystallographic textures labeled $\{011\}_z\langle100\rangle_x$ (±X_SS), $\{001\}_z\langle100\rangle_x$ (±XY_SS), and $\{111\}_z\langle2\overline{1}1\rangle_x$ (+120°Rot_SS) according to their preferred orientation components along the z and x directions. These textures arise from the ⟨100⟩ growth oriented along specific directions within the melt pool. For example, the $\{011\}_z\langle100\rangle_x$ texture formed under the ±X_SS condition is attributed to ⟨100⟩ growth along the ±45° directions within the melt-pool cross-section [27]. The formation of the other two textures follows the mechanisms reported previously [20]. At the melt-pool boundaries, the crystal orientations are inherited through epitaxial growth, thereby forming an overall single-crystal-like texture with well-aligned crystallographic orientations. Similar textures were observed for all the compositions (Supplementary Fig. S3), including the residual β phase of 6Cr in which α′ phase was detected by XRD. In the 6Cr specimen, the regions shown in black correspond either to non-β phases or to areas where the microstructure was so fine that Kikuchi line analysis could not be performed. The relationship between the scanning strategy and the resulting texture was consistent with that reported for Ti–15Mo–5Zr–3Al [20].

TEM analysis was conducted to identify phases that could not be detected XRD and EBSD. Fig. 4 shows the TEM images of the 6Cr alloy. The bright-field image reveals a fine needle-like microstructure Fig. 4 (a). Selected-area electron diffraction (SAED) along the [110] zone axis of the β phase confirmed the presence of not only the β and α′ phases detected by XRD, but also additional diffraction spots corresponding to the ω phase Fig. 4(a, d). The α′ phase exhibited two variants, α′₁ and α′₂, which shared a [0001] zone axis and differed in orientation by approximately 10°, in agreement with the Burgers orientation relationship between BCC and HCP. The dark-field images confirmed that the needle-like structures corresponded to the α′ phase Fig. 4(b1, b2). The ω phase was finely dispersed within the β matrix Fig. 4(c).

Increasing the Cr content stabilized the β phase, and no α′ phase was observed at Cr concentrations ≥ 12%. However, diffraction spots corresponding to the ω phase were detected within the β matrix in the 12Cr sample Fig. 5(a). These ω-spots became increasingly faint with further Cr addition Fig. 5(b-d). The addition of 3% Al to Cr-containing alloys almost completely inhibited the formation of the ω phase, resulting in a single-phase β structure Fig. 5(e-h).

3.3. Mechanical properties

Representative stress–strain curves are shown in Supplementary Fig. S4, and the yield strength, ultimate tensile strength, and plastic elongation values obtained from the curves are summarized in Fig. 6. The tensile loading direction was parallel to the BD, corresponding to ⟨110⟩, ⟨100⟩, and ⟨111⟩ for the ±X Scan, ±XY Scan, and +120° Rot Scan specimens, respectively. The 6Cr and 12Cr alloys, which contained α′ and/or ω phases, fractured with little to no plastic deformation; therefore, the recorded strength does not necessarily represent the yield stress. In contrast, the alloys containing ≥14Cr and the Al-containing alloys exhibited clear yielding and appreciable plastic deformation. Among them, specimens fabricated with ±X Scan and ±XY Scan, which induced ⟨110⟩ and ⟨100⟩ orientations, respectively, exhibited yield strengths of approximately 800 MPa, whereas those with ⟨111⟩

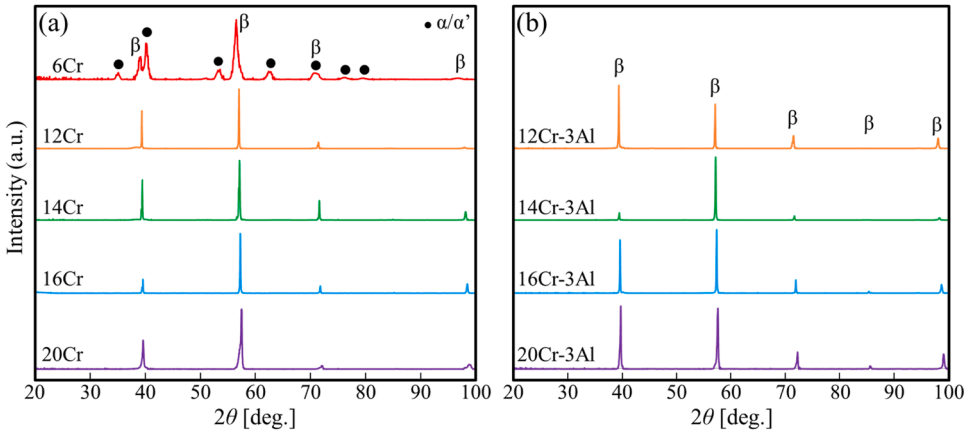

Fig. 2. XRD patterns of (a) Ti–Cr and (b) Ti–Cr–Al alloys. Peaks corresponding to the α′ phase were detected only in the 6Cr alloy, whereas the other alloys exhibited peaks that originated solely from the β phase.

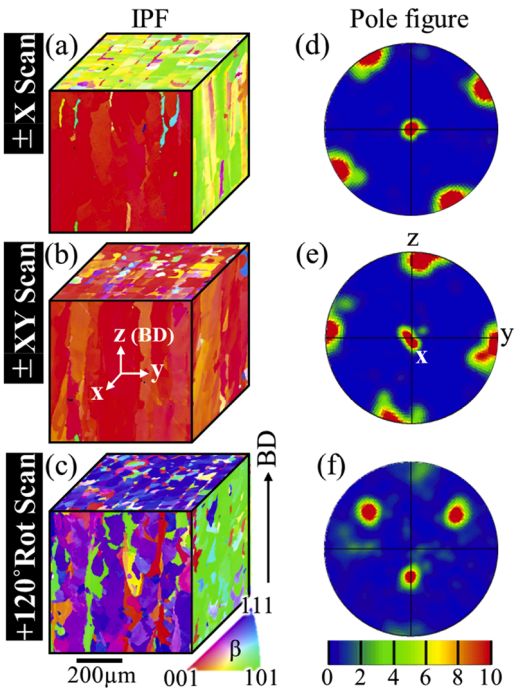

Fig. 3. (a–c) IPF maps showing the crystallographic orientation distributions along the normal directions of the three orthogonal planes, together with (d–f) the corresponding pole figures, for each scanning strategy. Depending on the scanning strategy, single-crystal-like textures with preferred orientations along the BD of ⟨110⟩, ⟨100⟩, and ⟨111⟩ were formed.

orientation formed by the +120° Rot Scan exceeded 900 MPa, which follows Schmid's law. Most of these ductile specimens exhibited limited strain hardening after yielding, with the flow stress remaining nearly constant or increasing slightly, indicating that deformation was dominated by dislocation slip [30].

Fig. 7 shows the variations in Young's modulus among the samples. The measured moduli exhibited good reproducibility, with the scatter among samples, defined as the standard deviation divided by the mean value, generally remaining below 0.1. Young's modulus showed pronounced orientation dependence in samples consisting of a single β phase, with the lowest values along the ⟨100⟩ orientation and highest values along ⟨111⟩. The lowest modulus was observed in the binary 16Cr and ternary 12Cr–3Al alloys, with the latter reaching approximately 60 GPa along the ⟨100⟩ direction (Fig. 7).

The variation in Young's modulus with respect to the *e/a* ratio is replotted for each crystallographic orientation in Fig. 8(a–c). The elastic anisotropy of Young's modulus, defined as the ratio of the maximum E_{111} to the minimum E_{100}, increased with decreasing *e/a* in the alloys with a single β phase (underlined in Fig. 8(d)), consistent with previous analyses of β-Ti single crystals [5]. An increase in Young's modulus accompanied by a reduction in anisotropy was observed in the 12Cr alloy, in which ω-phase formation was confirmed, and in the 6Cr alloy, which contained both ω and α′ phases.

4. Discussion

This study demonstrates the feasibility of tailoring both the crystallographic texture and phase constitution of Ti–Cr and Ti–Cr–Al alloys via in situ alloying in LPBF. By blending elemental powders and leveraging the process-specific features of LPBF, such as high cooling rates and localized heat input, we achieved precise compositional tuning and orientation control in additively manufactured parts. The resulting materials exhibited pronounced texture-dependent mechanical anisotropy as well as compositionally driven variations in phase stability and mechanical performance.

The present results clarify the processing–microstructure–property relationships governing LPBF-fabricated β-Ti alloys. Alloy composition, represented by Cr and Al contents and the resulting *e/a* ratio, determines the phase constitution by controlling the stability of the metastable β matrix and promotion or suppression of α′ and ω formation. In contrast, the scanning strategy determines the preferential crystallographic orientation along the BD, producing ⟨100⟩, ⟨110⟩, or ⟨111⟩ textures, which are largely preserved across the examined compositions. These two microstructural variables regulate the functional properties in distinct yet complementary ways: a single β phase prevents the modulus elevation associated with secondary-phase formation, whereas the ⟨100⟩ or ⟨111⟩ texture lowers the Young's modulus or increases yield strength, respectively. Thus, the combination of composition-based phase selection and scanning-strategy-based texture engineering provides a deliberate and predictable route for tuning the modulus–strength balance and

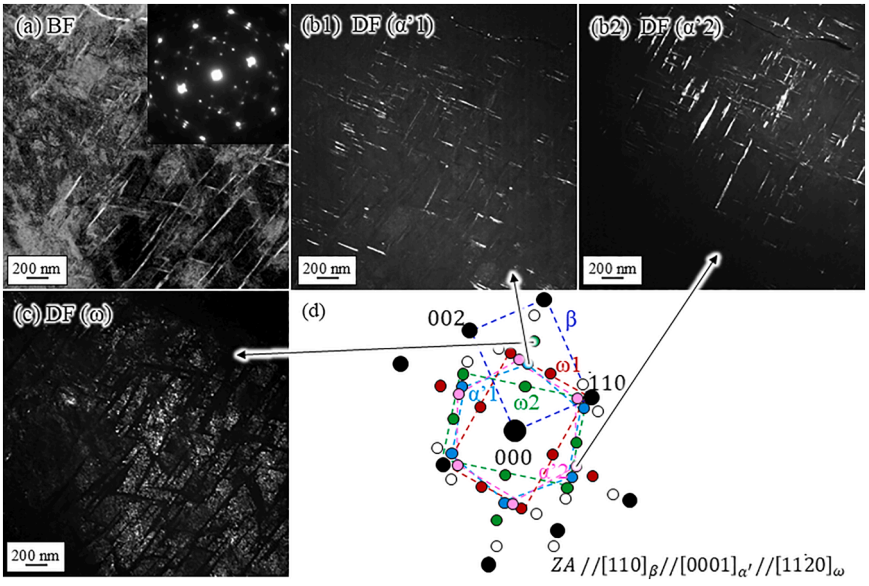

Fig. 4. (a) Bright-field TEM image and corresponding SAED pattern of the 6Cr alloy taken with the $[110]_{\beta}//[0001]_{\alpha'}//[11\bar{2}0]_{\omega}$ zone axis; (b1, b2) dark-field images of the α′ phase with different variants; (c) dark-field image of the ω phase; and (d) key diagram of the diffraction pattern.

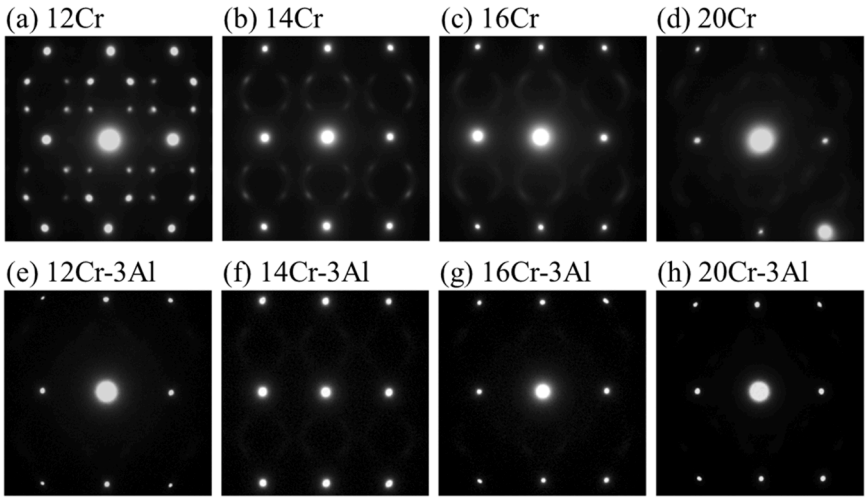

Fig. 5. Selected area electron diffraction patterns of each alloy taken along the $[110]_\beta$ zone axis. In the 12Cr alloy, distinct diffraction spots from the ω phase were observed, but these spots disappeared with increasing Cr content and with the addition of Al.

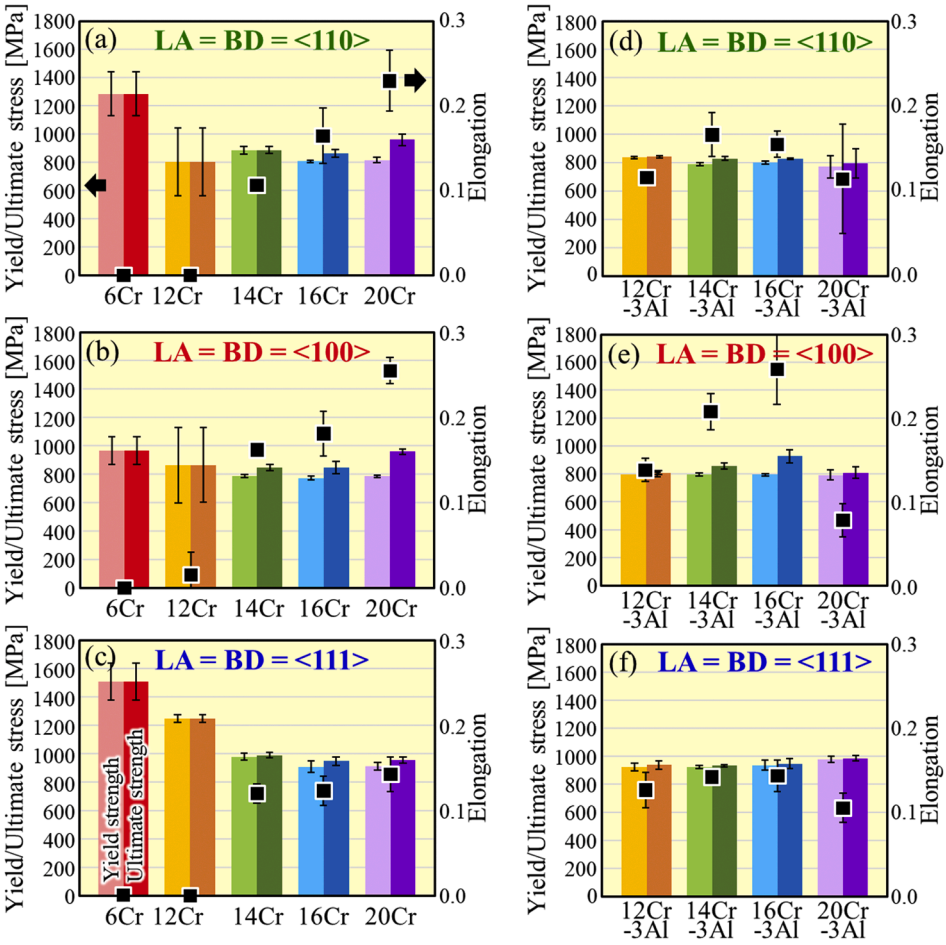

Fig. 6. Comparison of yield stress, ultimate stress, and elongation obtained from tensile tests for each alloy and scanning strategy (corresponding to preferred crystal orientation). The tensile loading axis (LA) was parallel to the BD indicated in Fig. 3.

enhancing the elastic admissible strain of LPBF-processed β-Ti alloys.

Achieving uniform properties requires thorough compositional homogenization, which is especially critical for metastable β-type Ti alloys, where phase stability is acutely sensitive to composition. One of the central challenges of in situ alloying is achieving truly homogeneous mixing of the elemental feed; if mixing is incomplete, a marble-like compositional heterogeneity can persist [31,32]. Although same-layer multiple exposures (remelting) are sometimes used to promote homogenization, they can also accelerate the evaporation of alloying elements, leading to composition shifts on the order of a few percent [33,34], which is particularly deleterious for Ti alloys, and partly diminish the rapid-turnaround advantage of AM. In this study, the melt-pool depth

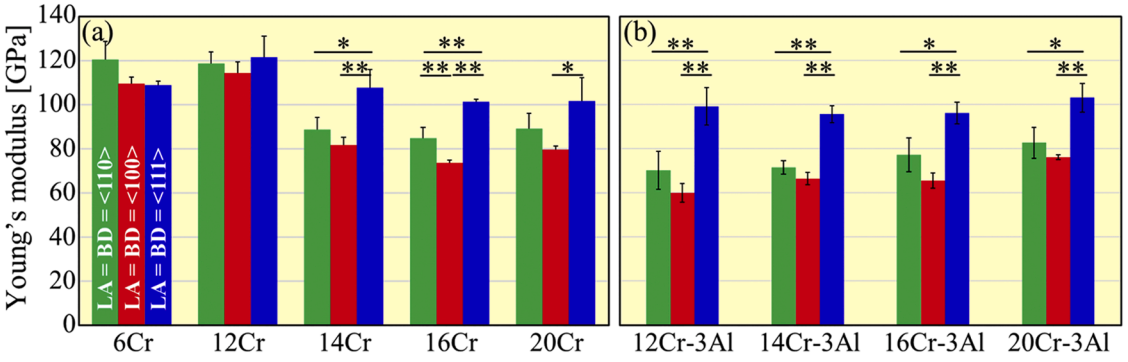

Fig. 7. Comparison of Young's modulus measured along the BD for each alloy and scanning strategy (preferred crystal orientation). Alloys exhibiting a single β phase showed clear elastic anisotropy, with the lowest modulus observed for the ⟨100⟩ orientation. **; $p < 0.01$, *; $p < 0.05$.

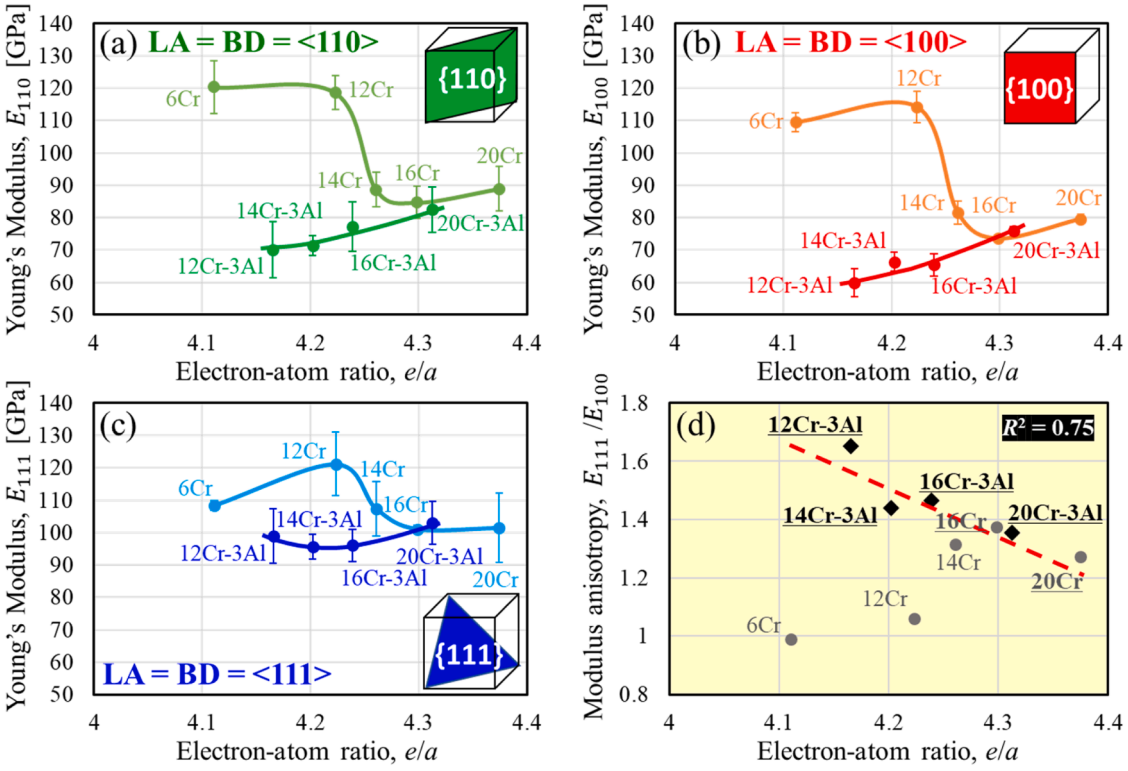

Fig. 8. (a–c) *e/a* dependence of Young's modulus plotted for each crystallographic orientation; (d) *e/a* dependence of Young's modulus anisotropy.

exceeded 300 μm (Supplementary Fig. S5), which was substantially larger than the layer thickness of 60 μm under the processing conditions. This choice of processing window, in which the melt-pool depth is much greater than the layer thickness [32,35], effectively subjects each volume element to multiple remelting events with extremely rapid convection [36,37], thereby promoting intensive stirring and yielding compositionally homogeneous alloying structure.

A key finding of this study is that the lowest Young's modulus (approximately 60 GPa) was obtained for the 12Cr–3Al ternary alloy when measured along the ⟨100⟩-oriented direction in the specimen exhibiting a ⟨100⟩//BD texture. For comparison, conventionally processed β-Ti alloys without a pronounced crystallographic texture generally exhibit Young's moduli of approximately 50–80 GPa [38]. Among Ti alloys with preferred ⟨100⟩ orientations (Table 3), a lower modulus of 43 GPa was reported for cold-rolled (Ti–35Nb)–4Sn (wt. %) [39]. Moreover, β-Ti single crystals exhibit Young's moduli of 36–44 GPa along the ⟨100⟩ direction [5,6,40,41], whereas LPBF-fabricated β-Ti alloys have shown values ranging from 44 to 85.7 GPa depending on

Table 3
Comparison of Young's modulus values reported for processed β-Ti single crystals [5,6,40,41] and LPBF-fabricated β-Ti alloys [15,18,42–44], with particular emphasis on measurements along the ⟨100⟩ crystallographic direction.

Specimen condition	Alloy	Young's modulus [GPa]
Single crystal, along ⟨100⟩	Ti–15Mo–5Zr–3Al (wt.%)	44.4
	$Ti_{70}Nb_{30}$ (at.%)	39.5
	Ti–26.6Nb–6.7Al (at.%)	36
	Ti–29Nb–13Ta–4.6Zr (wt.%)	35
As-built LPBF product, along ⟨100⟩-oriented direction	Ti–12Mo–6Zr–2Fe (wt.%)	85.7
	Ti–35Nb–7Zr–5Ta (wt.%)	60
	Ti–15Mo–5Zr–3Al (wt.%)	58.5
	Ti–22Zr–11Nb–2Sn (at. %)	51
	Ti–42Nb (wt.%)	44

alloy composition [15,18,42–44]. Although the value of approximately 60 GPa obtained for the ⟨100⟩-oriented Ti–12Cr–3Al alloy is not exceptionally low in absolute value, the significance of the present study lies in demonstrating an LPBF-specific methodology for tailoring the Young's modulus by simultaneously controlling the alloy composition (phase stability) and crystallographic texture. The reduced modulus along ⟨100⟩ originates from the intrinsic elastic anisotropy of the BCC β phase [5], confirming the effectiveness of scanning-strategy-based texture control in tailoring directional elastic properties. Future studies can extend this strategy to Nb-based β-Ti alloys, which tend to exhibit particularly low Young's moduli. Using Nb-containing feedstocks for in situ alloying during LPBF therefore represents a promising strategy for further reducing the elastic modulus. However, achieving homogeneous alloying will require careful optimization of the processing conditions because Nb has a substantially higher melting point (2468 °C) than Ti.

It should also be noted that the LPBF-induced texture obtained in this study was not perfectly single crystalline because the {100} pole retained a finite angular spread. According to the single-crystal data reported by Tane et al. [5], further sharpening the ⟨100⟩ texture of Ti–12Cr–3Al (e/a = 4.17) toward an ideal single-crystal orientation could potentially reduce its Young's modulus to 40 GPa. In a previous study on LPBF-processed Ti–15Mo–5Zr–3Al alloys [18], the single-crystal elastic stiffness components were accurately extracted from the macroscopic elastic stiffness of textured LPBF specimens using an inverse self-consistent (iSC) approximation, considering the EBSD-derived crystallographic orientation distribution and grain morphology [45]. This approach effectively separates the influence of the crystallographic orientation spread and intergranular elastic interactions from the measured macroscopic response to determine the intrinsic single-crystal elasticity. Furthermore, comparing the experimentally measured response with that reconstructed from the extracted single-crystal stiffness enables quantitative evaluation of the extent to which the texture spread attenuates the elastic anisotropy. This approach can be extended to the present Ti–Cr–Al alloys to clarify the relationships between texture spread and mechanical anisotropy and to determine the practically achievable lower bound of the Young's modulus.

The transferability of the proposed texture control strategy to complex geometries requires further investigation. Because crystallographic texture formation during LPBF is governed by the local melt-pool geometry and thermal gradients, variations in component cross-sectional area, underlying structure, scan-path length, and local heat-dissipation conditions may alter the melt-pool shape and solidification process, resulting in spatially varying texture intensity and orientation spread. Therefore, maintaining a sufficiently sharp and homogeneous texture throughout a complex component requires location-specific optimization of laser processing conditions to establish favorable melt-pool geometries and thermal gradients for texture formation. Melt-pool simulations play an essential role in guiding such local process optimization, and extending their application to complex geometries represents an important direction for future work.

Typically, the elastic performance of metallic materials is assessed by the ratio of the yield strength to Young's modulus, often referred to as the elastic admissible strain; a higher value indicates superior elastic accommodation and serves as a key metric of biomechanical compatibility for orthopedic applications [46,47]. Fig. 9 compares the elastic admissible strain obtained in this study, resolved by composition and preferred crystallographic orientation, with the reported range for LPBF-fabricated Ti-6Al-4V, a widely used implant alloy. Overall, the Ti–Cr and Ti–Cr–Al builds exhibited greater biomechanical compatibility than Ti-6Al-4V; in particular, the ⟨100⟩-textured Ti–Cr–Al showed an excellent strength–modulus balance. Therefore, the texture-engineered LPBF alloys developed in this study are promising candidates for biomedical implants.

Interestingly, in the Ti–Cr binary system, the Cr concentration

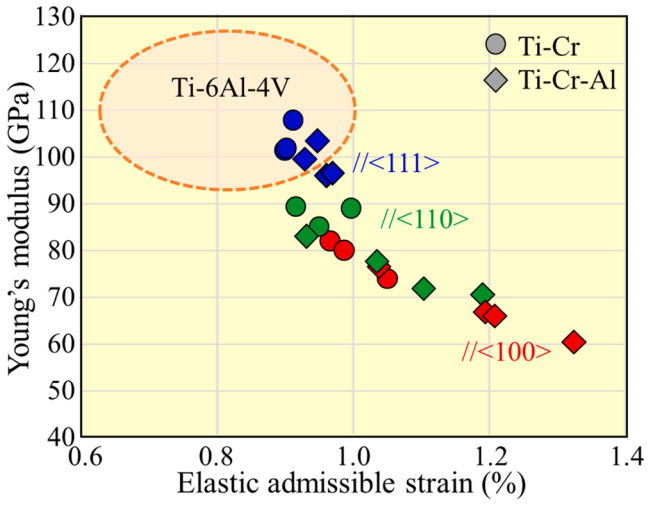

Fig. 9. Relationship between Young's modulus and elastic admissible strain. For reference, the reported range for LPBF-fabricated Ti–6Al–4V is also included.

corresponding to the lowest Young's modulus in the LPBF-fabricated materials (16Cr) differed from that reported for conventionally cast materials (12Cr) [22]. This reflects a shift of the compositional region for ω-phase formation toward the higher Cr side, leading to the formation of the ω phase in the LPBF material at 12Cr, whereas it did not form at this composition in the cast material. This discrepancy highlights the influence of the processing route on phase stability and elastic response. Specifically, the LPBF process alters the stability of the metastable β phase through its unique thermomechanical history, thereby shifting the compositional window for ω-phase formation. Consequently, alloy compositions optimized for conventional processing cannot be directly transferred to LPBF without considering these process-induced changes in phase stability.

The oxygen content, which can significantly affect phase stability and thus ω-phase precipitation, was comparable between the present study and a previous report (~0.1 wt.%) [22]; therefore, variations in oxygen content are unlikely to be the dominant factor responsible for this ω-phase precipitation. Zhao et al. [22] reported that a deformation-induced ω phase was observed in cold-rolled cast 12Cr alloys following solution treatment. In contrast, alloys with ≥13Cr did not exhibit such transformations, indicating a critical threshold for β-phase stability in the cast material.

For the as-built 12Cr specimen, in which the ω phase was detected, heat treatment at 900 °C for 1 h followed by ice-water quenching resulted in the disappearance of the ω-phase diffraction spots (Supplementary Fig. S6), indicating that the nominal 12Cr composition does not intrinsically form the ω phase during conventional quenching. Therefore, the formation of ω phase in the as-built material is attributed to the unique thermomechanical history associated with the LPBF process rather than to alloy composition alone. The tensile residual stress of 353 MPa measured in the as-built specimen (Fig. 10) suggests the presence of a substantial mechanical driving force, which may have promoted the ω-phase formation in the metastable β matrix. For a Ti–20V alloy with a metastable β phase, such ω transformation has been reported under stresses below 400 MPa [48]. Other process-related factors, including extremely rapid solidification, repeated thermal cycling, local reheating during successive melting and remelting events, and a high density of lattice defects, may also influence the transformation. Comparable process-dependent changes in phase constitution and transformation behavior have been reported in other LPBF-processed metastable β-Ti alloys, where repeated thermal cycling or variations in LPBF parameters altered ω-phase development, β-phase stability, and the activation of TRIP/TWIP mechanisms [49–51]. Although no pronounced

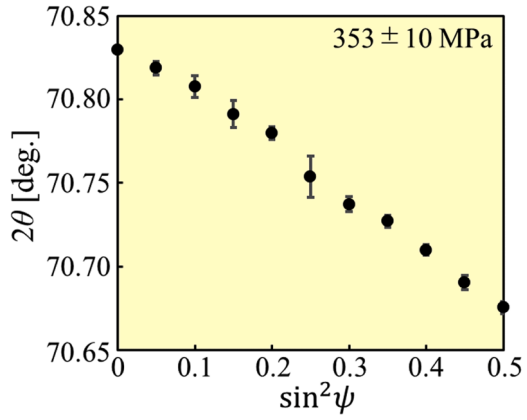

Fig. 10. $\mathrm{Sin}^2\psi$-plots for residual stress σ_z.

compositional heterogeneity was detected by EDS, nanoscale compositional fluctuations [52] below the spatial resolution of the analysis could not be completely excluded. Therefore, the ω phase observed in the as-built 12Cr alloy is likely attributable to the combined effects of marginal β-phase stability and the complex thermomechanical history during the LPBF process. Accordingly, within the well-established W-shaped relationship between Young's modulus and the *e/a* ratio, the apparent onset of ω-phase formation shifted toward higher *e/a* values under the thermomechanical conditions imposed by LPBF (Fig. 11).

It should also be noted that the residual stress state may vary with the scanning strategy and the resulting crystallographic texture. Previous LPBF studies have demonstrated that changes in scanning strategy and build orientation can modify the local heat flow, thermal cycling, mechanical constraints, and interactions with the machine-specific process environment, thereby producing distinct residual stress distributions [53,54]. In addition, in strongly textured materials, crystallographic elastic anisotropy may affect elastic stress partitioning and diffraction-based evaluation of residual stress [55]. As the scanning strategy simultaneously determines the process-specific thermal history and crystallographic texture, their respective contributions to the residual stress state cannot be separated from the present measurements.

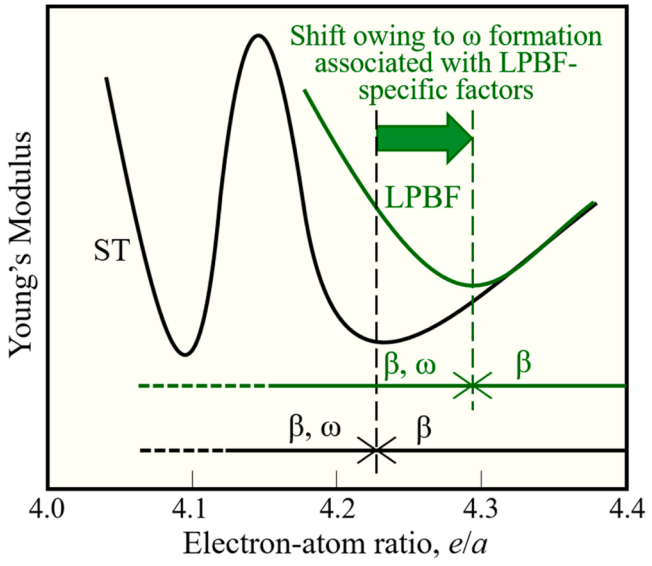

Fig. 11. Schematic representation of a possible LPBF-induced shift in the compositional range for ω-phase formation. Process-specific factors, including residual stress and repeated thermal cycling, may promote ω formation in a metastable β matrix and thereby increase Young's modulus.

Systematic investigations using geometrically identical, unmachined, as-built specimens fabricated under different scanning strategies are therefore required. These studies should be combined with texture-resolved diffraction analysis and thermomechanical modeling to clarify the respective roles of processing history and texture in residual stress development. The ultimate goal is to identify an optimal scanning-strategy/texture combination that maintains the desired low modulus while effectively controlling residual stress and other LPBF-specific factors that may influence ω-phase formation.

From a broader viewpoint, the present results indicate that conventional design maps that correlate Young's modulus with the *e/a* ratio, which are primarily based on cast or wrought alloys in a near-equilibrium or stress-relieved condition [3–5,22], cannot be directly applied to LPBF-processed β-Ti alloys. In LPBF, the combined effects of process-induced stresses and thermal history on a metastable β matrix may shift the apparent β→ω transformation boundary and, consequently, the composition range in which a low modulus can be retained. In other words, the "safe" *e/a* window that avoids ω formation is not an intrinsic material constant, but is process-dependent and, in particular, sensitive to the magnitude and distribution of internal stresses. Therefore, a natural extension of the present work is the construction of an AM process-aware design map in which *e/a* (or $\mathrm{Mo_{eq}}$) is combined with the descriptors of the scanning-strategy-dependent thermal history, residual stress state, and crystallographic texture. Such a map would allow the stability of the metastable β phase to be assessed under the specific thermomechanical conditions imposed by LPBF, electron beam-PBF, or subsequent mechanical processing, rather than assuming a single, universal W-shaped *e/a–E* relationship. From a practical viewpoint, such an AM process-aware framework would also provide a useful guideline for alloy screening because promising compositions could be selected not only on the basis of their intrinsic thermodynamic stability but also with respect to their tolerance to process-induced stresses and local thermal histories in real components. The proposed AM process-aware design framework is shown in Fig. 12.

The sensitivity of metastable β-Ti alloys to the LPBF processing history is not unique to the Ti–Cr system. In LPBF-processed Ti–10V–2Fe–3Al, repeated heating and cooling cycles were reported to promote early-stage solute partitioning and isothermal ω precipitation, thereby suppressing TRIP/TWIP and reducing ductility in the as-built specimen; subsequent β-solution treatment and quenching reactivated these deformation mechanisms [49]. In the same nominal alloy system, variations in the LPBF parameters were shown to modify the ω-phase density and β-phase stability, thereby changing the active deformation mechanisms and the resulting strength–ductility balance [50]. Similarly, repeated track- and layer-wise thermal cycling promoted the development of isothermal ω in LPBF-processed Ti–13.5Mo, whereas Sn addition retarded its evolution toward the commensurate form and mitigated the associated embrittlement [51]. Together with reports of deformation-induced ω-phase formation in conventionally processed metastable β-Ti alloys [48,56–58], these studies indicate that the transformation behavior of metastable β-Ti alloys can be affected by both alloy chemistry and the process-specific thermal and mechanical history.

The ω phase exhibits a higher Young's modulus compared with the β phase, and orientation-dependent elastic properties. The ω phase precipitates in the β matrix as four crystallographically equivalent variants following the $(0001)_\omega//\{111\}_\beta$ and $\langle 11\bar{2}0\rangle_\omega//\langle 1\bar{1}1\rangle_\beta$ crystallographic orientation relationship with respect to the β phase. Its precipitation increases the Young's modulus of the alloy while reducing the overall elastic anisotropy. Indeed, in the 12Cr alloy, a marked increase in Young's modulus and a reduction in anisotropy were observed, although a weak trend associated with the elastic anisotropy of the β phase was still retained (Fig. 7(a)). Similarly, the α′ phase has a higher Young's modulus than the β phase and exhibits anisotropy in Young's modulus. Because the α′ phase forms in the β matrix as 24 crystallographically

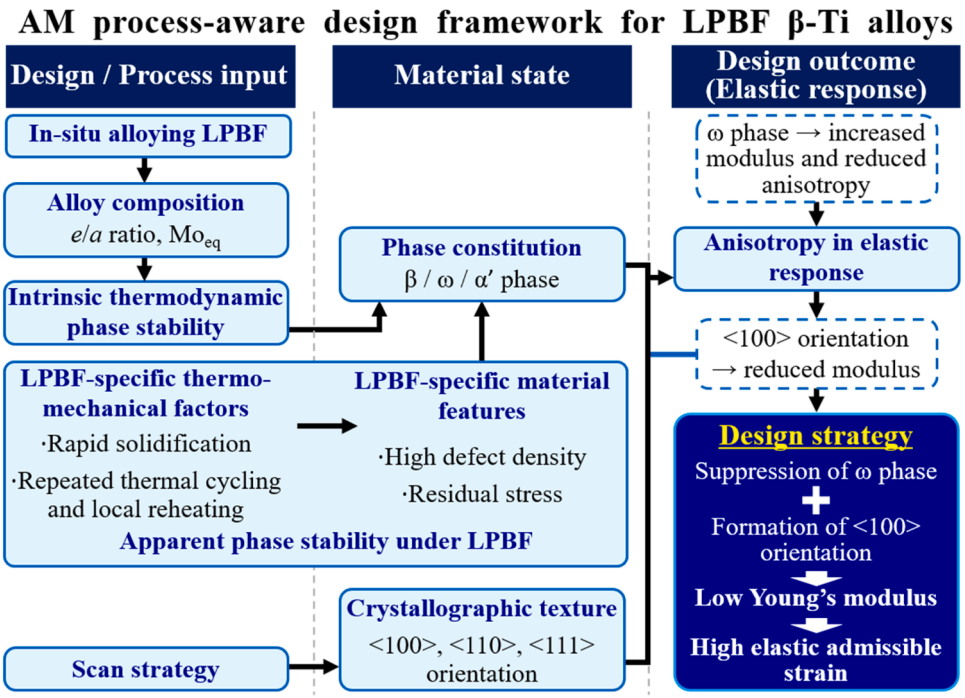

Fig. 12. Schematic illustration of the AM process-aware design framework proposed for LPBF-fabricated β-Ti alloys. Alloy composition determines the intrinsic β-phase stability, whereas LPBF-specific thermo-mechanical factors, including rapid solidification, repeated thermal cycling and local reheating, and the resultant high defect density and residual stress, may modify the apparent phase stability and ω-phase formation tendency. Independently, the scan strategy controls the crystallographic texture. The resulting phase constitution and crystallographic texture jointly determine the directional elastic response. Suppression of the ω phase combined with formation of the elastically compliant ⟨100⟩ orientation provides a pathway toward a low Young's modulus and thus high elastic admissible strain defined as yield strength/Young's modulus.

equivalent variants following the $(0001)_{\alpha'}//\{110\}_{\beta}$ and $\langle 11\bar{2}0\rangle_{\alpha'}//\langle 1\bar{1}1\rangle_{\beta}$ orientation relationship with respect to the β phase, its formation is expected to reduce the anisotropy more significantly. Therefore, the reduced anisotropy observed in the Ti–6Cr and Ti–12Cr alloys in Fig. 7(a) can be explained by the formation of secondary phases.

The near absence of plasticity observed in the 12Cr alloy is consistent with the well-established embrittling effect of the ω phase [59]. However, the individual contribution of the ω phase cannot be fully separated from other LPBF-related effects based on the present results. Because oxygen contents were comparable among the examined alloys and similar scanning-strategy-dependent textures were obtained across different compositions, neither oxygen content nor texture is likely to be the primary cause of the marked reduction in plasticity. Therefore, from a biomedical perspective, suppressing ω-phase formation is important to maintain a low modulus and enhance plasticity. Three possible strategies can be considered to mitigate ω-phase formation in LPBF materials. First, the addition of Al has been shown to strongly suppress deformation-induced ω formation [48]. In this study, although the 12Cr alloy exhibited clear ω-phase precipitation, the 12Cr–3Al alloy showed no detectable ω formation and retained a low Young's modulus, which is consistent with the suppressive role of Al in ω-phase formation. In fact, in LPBF specimens of the Al-containing metastable β titanium alloy Ti–15Mo–5Zr–3Al, the formation of the ω phase is rarely observed [18]. Sn has also been reported, similarly to Al, to suppress the precipitation of the ω phase in LPBF-processed Ti–Cr and Ti–Mo alloys and thereby inhibit the increase in Young's modulus [51,60]. The second approach involves the optimization of the processing conditions. Lowering the laser power (e.g., to 75 W) during LPBF significantly reduced the residual stress to below 100 MPa [61]. Alternatively, electron beam powder bed fusion (EB-PBF), another PBF-based method, inherently minimizes residual stress [61,62] and can also promote the ⟨100⟩//BD texture [63], despite the lack of active orientation-direction control. However, because EB-PBF requires high-temperature preheating, it remains to be determined whether the metastable β phase, and thus the associated low modulus, can be maintained without triggering equilibrium phase transformations or isothermal ω formation. Third, post-processing annealing may eliminate the ω phase. However, if annealing degrades the deliberately engineered crystallographic texture through recrystallization or grain growth, the low Young's modulus along the ⟨100⟩ direction is lost. Therefore, the influence of such heat treatments should be investigated in a separate study.

The findings of this study have important implications for the design of low-modulus Ti alloys fabricated via LPBF. While the intrinsic anisotropy and composition-processing tunability of LPBF provide valuable tools, the complex interplay between residual stress and phase stability must be carefully managed. In this regard, in situ alloying is a powerful strategy that enables fine compositional tuning without the need for pre-alloyed powders, facilitating the rapid screening of stability boundaries and identification of compositions that resist undesirable phase transformations.

The cellular microstructure introduced by rapid solidification is a strengthening factor specific to alloys fabricated by LPBF. These cells are submicron-sized structures that have been widely reported in LPBF specimens of Ni-based superalloys [64,65], stainless steels [66,67], and high-entropy alloys [67,68]. They are characterized by solute segregation and dislocation accumulation within the segregated regions. These cells markedly increase the strength of LPBF products. For example, in the Ni-based alloy Inconel 718, the presence of cells has been reported to increase the yield strength by as much as 40%, as revealed by heat treatments that eliminate cellular microstructures (elemental segregation and dislocation accumulation) [69]. In contrast, for the present alloy, the strength is comparable to that of the previously reported cast material [22], indicating that the effect of the cells is minimal.

The STEM bright-field image Fig. 13(a) shows no dislocation accumulation, and the STEM–EDS analysis Fig. 13(b, c) does not reveal any

detectable concentration modulation, as reported for Ni-based superalloys and stainless steels. Supplementary Fig. S7 shows the segregation and dislocation accumulation structures observed in the LPBF-processed Inconel 718 alloy for comparison. According to the Ti–Cr phase diagram, on the Ti-rich side, the liquidus and solidus lines are relatively close, suggesting that the present composition may be inherently less prone to segregation.

Furthermore, controlling crystallographic orientation through scanning strategies broadens the design space beyond composition alone. As demonstrated in this study, specimens with dominant ⟨100⟩, ⟨110⟩, and ⟨111⟩ orientations exhibited distinct mechanical responses, and texture control proved to be highly effective in achieving anisotropy in Young's modulus and strength. In addition to the simple selection of crystallographic orientation, the high degree of freedom in locally assigning processing conditions within a single AM-built component enables "patchwork-like" combinations of textures that can be tailored to the mechanically required properties at each specific location, even when using a single material [20]. Although multimaterial AM [70] is also being explored for this purpose in the context of biomaterials, where corrosion must be strictly avoided, the potential for galvanic corrosion arising from compositional differences at multimaterial interfaces [71] is a serious concern. In contrast, site-specific tailoring of the mechanical properties within a single material is highly attractive for biomedical applications. Thus, this approach opens a new pathway for the design of advanced biomaterials.

5. Conclusions

In this study, we fabricated nine compositions of Ti–Cr and Ti–Cr–Al alloys via in situ alloying to eliminate the need for pre-alloyed powders. Additionally, we implemented crystallographic texture control using tailored scanning strategies. The following results were obtained regarding phase stability, microstructure, and mechanical properties:

1. By employing processing conditions that produced a melt-pool depth substantially greater than the layer thickness, we promoted multiple remelting events and achieved compositionally homogeneous builds.
2. For all compositions, single-crystal-like textures commensurate with the symmetry of the scan strategy were achieved.
3. At 12Cr, the ω phase was detected in the as-built material but disappeared after solution treatment and ice-water quenching, indicating that ω-phase formation is associated with the LPBF-specific thermomechanical history. Residual stress is considered one plausible contributor, together with other factors inherent to the LPBF process, such as rapid solidification, repeated thermal cycling, local reheating, and high defect density.
4. The single-β-phase specimens exhibited pronounced elastic anisotropy. In the ⟨100⟩ direction, the lowest modulus (approximately 60 GPa) was recorded for 12Cr–3Al, which exhibited the lowest e/a value among the examined alloys.
5. The yield strength, which depends on the texture, ranged from 800 to 1000 MPa. The resulting elastic admissible strain exceeded 1.3% in the ⟨100⟩-oriented 12Cr–3Al, surpassing the reported values for LPBF Ti–6Al–4V and underscoring the biomedical potential of these alloys.

Taken together, the present Ti–Cr and Ti–Cr–Al results provide the basis for an AM process-aware design framework that integrates composition-driven phase stability, LPBF-specific thermomechanical history, and scan-strategy-controlled crystallographic texture to guide the development of low-modulus, high-strength metastable β-Ti alloys.

CRediT authorship contribution statement

Takuya Ishimoto: Writing – review & editing, Writing – original draft, Validation, Methodology, Investigation, Funding acquisition, Formal analysis. **Soki Hoshino:** Visualization, Investigation. **Yuki Nishikawa:** Visualization, Investigation. **Masakazu Tane:** Validation, Investigation. **Kazuhisa Sato:** Visualization, Investigation. **Hyoung Seop Kim:** Validation, Supervision. **Takayoshi Nakano:** Writing – review & editing, Supervision, Project administration, Funding acquisition, Conceptualization.

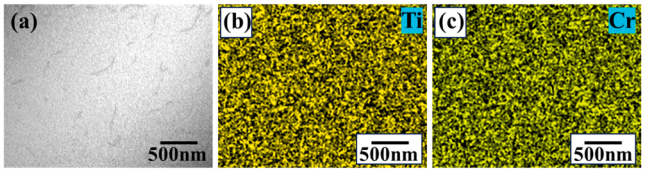

Fig. 13. (a) STEM bright-field image and corresponding STEM-EDS maps of (b) Ti and (c) Cr for the 16Cr specimen.

Declaration of competing interest

The authors declare that they have no known competing financial interests or personal relationships that could have appeared to influence the work reported in this paper.

Acknowledgments

This work was supported by Grant-in-Aid for Transformative Research Area (A) [JP21H05197] from the Japan Society for the Promotion of Science, CREST-Nanomechanics [JPMJCR2194] from the Japan Science and Technology Agency, and research funding from the Light Metal Educational Foundation. The authors express their sincere gratitude to Mr. K. Kimura of the Technical Division, Graduate School of Engineering, The University of Osaka, for his valuable technical support during this study.

Supplementary materials

Supplementary material associated with this article can be found, in the online version, at doi:10.1016/j.actamat.2026.122715.

Data availability

The data will be made available upon request.

References

[1] Y. Gao, W. Jiang, D. Zeng, X. Liang, C. Ma, W. Xiao, Additive manufacturing of titanium alloys for biomedical applications: a systematic review, Rev. Mater. Res. 1 (2025) 100011, https://doi.org/10.1016/j.revmat.2025.100011.
[2] H.N. Singh, S. Agrawal, Y.K. Modi, Additively manufactured patient specific implants: a review, Arch. Mech. Eng. 71 (2024) 109–138, https://doi.org/10.24425/ame.2024.149635.
[3] P. Raja, K.B. Babu, R. Kannan, V. Shanmugam, N.S. Balaji, R. Sahani, L. Behera, A. Pugazhenthi, M.R. Thansekhar, Progress in the optimization of compositional design and thermomechanical processing of metastable β Ti alloys for biomedical applications, ACS Biomater. Sci. Eng. 10 (2024) 3528–3547, https://doi.org/10.1021/acsbiomaterials.3c01912.
[4] J. Pesode, S. Barve, A review—Metastable β titanium alloy for biomedical applications, J. Eng. Appl. Sci. 70 (2023) 25, https://doi.org/10.1186/s44147-023-00196-7.
[5] M. Tane, S. Akita, T. Nakano, K. Hagihara, Y. Umakoshi, M. Niinomi, H. Nakajima, Peculiar elastic behavior of Ti–Nb–Ta–Zr single crystals, Acta Mater. 56 (2008) 2856–2863, https://doi.org/10.1016/j.actamat.2008.02.017.
[6] S.-H. Lee, M. Todai, M. Tane, K. Hagihara, H. Nakajima, T. Nakano, Biocompatible low Young's modulus achieved by strong crystallographic elastic anisotropy in Ti–15Mo–5Zr–3Al alloy single crystal, J. Mech. Behav. Biomed. Mater. 14 (2012) 48–54, https://doi.org/10.1016/j.jmbbm.2012.05.005.
[7] S. Liang, Review of the design of titanium alloys with low elastic modulus as implant materials, Adv. Eng. Mater. 22 (2020) 2000555, https://doi.org/10.1002/adem.202000555.
[8] Y.S. Kim, O. Gokcekaya, A. Matsugaki, R. Ozasa, T. Nakano, Laser energy-dependent processability of non-equiatomic TiNbMoTaW high-entropy alloy

through in-situ alloying of elemental feedstock powders by laser powder bed fusion, Materialia 38 (2024) 102241, https://doi.org/10.1016/j.mtla.2024.102241.
[9] H. Zhang, Y. Hou, X. Wang, X. Li, Y. He, F. Li, Y. Lu, H. Su, High throughput in-situ synthesis of Fe–Cr–Ni alloys via laser powder bed fusion: exploring the microstructure and property evolution, Addit. Manuf. 81 (2024) 103996, https://doi.org/10.1016/j.addma.2024.103996.
[10] N. Nohira, C. Chen, Y. Jin, W.T. Chiu, A. Umise, T. Teramoto, M. Tahara, R. Ozasa, T. Ishimoto, Y. Koizumi, T. Nakano, H. Hosoda, Introducing a novel fabrication route for metastable β-type Ti-Cr-Sn alloys with ultra-high Sn content using pure elemental mixed powders via laser powder bed fusion, Addit. Manuf. 124 (2026) 105213, https://doi.org/10.1016/j.addma.2026.105213.
[11] T. Shu, J. Yuan, F. Liu, W. Shen, G.J. Cheng, In-situ alloying and microstructural control in high entropy alloys with nano-carbide-framework via powder bed fusion, Addit. Manuf. 104 (2025) 104766, https://doi.org/10.1016/j.addma.2025.104766.
[12] T. Ishimoto, K. Hagihara, K. Hisamoto, T. Nakano, Stability of crystallographic texture in laser powder bed fusion: understanding the competition of crystal growth using a single crystalline seed, Addit. Manuf. 43 (2021) 102004, https://doi.org/10.1016/j.addma.2021.102004.
[13] K. Hagihara, T. Nakano, Control of anisotropic crystallographic texture in powder bed fusion additive manufacturing of metals and ceramics—A review, JOM 74 (2022) 1760–1773, https://doi.org/10.1007/s11837-021-04966-7.
[14] X. Qi, X. Liang, J. Wang, H. Zhang, X. Wang, Z. Liu, Microstructure tailoring in laser powder bed fusion (L-PBF): strategies, challenges, and future outlooks, J. Alloys Compd. 970 (2024) 172564, https://doi.org/10.1016/j.jallcom.2023.172564.
[15] S. Pilz, T. Gustmann, F. Günther, M. Zimmermann, U. Kühn, A. Gebert, Controlling the Young's modulus of a ß-type Ti-Nb alloy via strong texturing by LPBF, Mater. Des. 216 (2022) 110516, https://doi.org/10.1016/j.matdes.2022.110516.
[16] W.C. Batalha, R.L. Batalha, K. Kosiba, C.S. Kiminami, P. Gargarella, Effect of scanning strategy on microstructure and mechanical properties of a biocompatible Ti–35Nb–7Zr–5Ta alloy processed by laser-powder bed fusion, J. Mater. Res. 38 (2023) 154–164, https://doi.org/10.1557/s43578-022-00735-7.
[17] T. Ishimoto, R. Suganuma, T. Nakano, Tailoring the crystallographic texture of biomedical metastable β-type Ti-alloy produced via laser powder bed fusion using temperature-field simulations, Mater. Lett. 349 (2023) 134835, https://doi.org/10.1016/j.matlet.2023.134835.
[18] S. Higashino, D. Miyashita, T. Ishimoto, E. Miyoshi, T. Nakano, M. Tane, Low Young's modulus in laser powder bed fusion processed Ti–15Mo–5Zr–3Al alloys achieved by the control of crystallographic texture combined with the retention of low-stability bcc structure, Addit. Manuf. 102 (2025) 104720, https://doi.org/10.1016/j.addma.2025.104720.
[19] A. Keshavarzkermani, R. Esmaeilizadeh, U. Ali, P.D. Enrique, Y. Mahmoodkhani, N.Y. Zhou, A. Bonakdar, E. Toyserkani, Controlling mechanical properties of additively manufactured Hastelloy X by altering solidification pattern during laser powder-bed fusion, Mater. Sci. Eng. A 762 (2019) 138081, https://doi.org/10.1016/j.msea.2019.138081.
[20] T. Ishimoto, N. Morita, R. Ozasa, A. Matsugaki, O. Gokcekaya, S. Higashino, M. Tane, T. Mayama, K. Cho, H.Y. Yasuda, M. Okugawa, Y. Koizumi, M. Yoshiya, D. Egusa, T. Sasaki, E. Abe, H. Kimizuka, N. Ikeo, T. Nakano, Superimpositional design of crystallographic textures and macroscopic shapes via metal additive manufacturing—Game-change in component design, Acta Mater. 286 (2025) 120709, https://doi.org/10.1016/j.actamat.2024.120709.
[21] P.J. Bania, Beta titanium alloys and their role in the titanium industry, JOM 46 (1994) 16–19, https://doi.org/10.1007/BF03220742.
[22] X. Zhao, M. Niinomi, M. Nakai, J. Hieda, T. Ishimoto, T. Nakano, Optimization of Cr content of metastable β-type Ti–Cr alloys with changeable Young's modulus for spinal fixation applications, Acta Biomater. 8 (2012) 2392–2400, https://doi.org/10.1016/j.actbio.2012.03.037.
[23] G. Shao, P. Tsakiropoulos, Prediction of ω phase formation in Ti–Al–X alloys, Mater. Sci. Eng. A 329-331 (2002) 914–919, https://doi.org/10.1016/S0921-5093(01)01576-3.
[24] F. Brumbauer, N.L. Okamoto, T. Ichitsubo, W. Sprengel, M. Luckabauer, Minor additions of Sn suppress the omega phase formation in beta titanium alloys, Acta Mater. 262 (2024) 119466, https://doi.org/10.1016/j.actamat.2023.119466.
[25] H. Matsumoto, S. Watanabe, N. Masahashi, S. Hanada, Composition dependence of young's modulus in Ti-V, Ti-Nb, and Ti-V-Sn alloys, Metall. Mater. Trans. A 37 (2006) 3239–3249, https://doi.org/10.1007/BF02586159.
[26] Y.L. Hao, S.J. Li, S.Y. Sun, C.Y. Zheng, R. Yang, Elastic deformation behaviour of Ti–24Nb–4Zr–7.9Sn for biomedical applications, Acta Biomater. 3 (2007) 277–286, https://doi.org/10.1016/j.actbio.2006.11.002.
[27] T. Ishimoto, K. Hagihara, K. Hisamoto, S.-H. Sun, T. Nakano, Crystallographic texture control of beta-type Ti–15Mo–5Zr–3Al alloy by selective laser melting for the development of novel implants with a biocompatible low Young's modulus, Scr. Mater. 132 (2017) 34–38, https://doi.org/10.1016/j.scriptamat.2016.12.038.
[28] ASTM International, Standard Test Method for Verifying the Alignment of X-Ray Diffraction Instrumentation for Residual Stress Measurement, in: ASTM E915-96 (2002), ASTM International, West Conshohocken, PA, 2002, https://doi.org/10.1520/E0915-96R02.
[29] G. Li, H. Guo, L. Li, C. Wang, J. Zheng, W. Tian, H. Li, X. Li, Purification of terbium by means of argon and hydrogen plasma arc melting, J. Alloys Compd. 659 (2016) 1–7, https://doi.org/10.1016/j.jallcom.2015.10.180.
[30] C. Qiu, Q. Liu, R. Ding, Significant enhancement in yield strength for a metastable beta titanium alloy by selective laser melting, Mater. Sci. Eng. A 816 (2021) 141291, https://doi.org/10.1016/j.msea.2021.141291.
[31] M.H. Mosallanejad, B. Niroumand, A. Aversa, D. Manfredi, A. Saboori, Laser powder bed fusion in-situ alloying of Ti-5%Cu alloy: process-structure relationships, J. Alloys Compd. 857 (2021) 157558, https://doi.org/10.1016/j.jallcom.2020.157558.
[32] R. Duan, S. Li, B. Cai, Z. Tao, W. Zhu, F. Ren, M.M. Attallah, In situ alloying based laser powder bed fusion processing of β Ti–Mo alloy to fabricate functionally graded composites, Compos. B: Eng. 222 (2021) 109059, https://doi.org/10.1016/j.compositesb.2021.109059.
[33] A. Chmielewska, B. Wysocki, J. Buhagiar, B. Michalski, B. Adamczyk-Cieślak, M. Gloc, W. Święszkowski, In situ alloying of NiTi: influence of laser powder bed fusion (LBPF) scanning strategy on chemical composition, Mater. Today Commun. 30 (2022) 103007, https://doi.org/10.1016/j.mtcomm.2021.103007.
[34] J. Zeng, Y. Yang, H. Peng, P. Wang, C. Liu, Z. Chen, W. Chen, X. Liu, Y. Wu, Z. Liu, Z. Lu, Additive manufacturing of high entropy shape memory alloy with outstanding properties through multi-remelting in-situ alloying, Addit. Manuf. 88 (2024) 104253, https://doi.org/10.1016/j.addma.2024.104253.
[35] Y.S. Kim, O. Gokcekaya, A. Matsugaki, R. Ozasa, T. Nakano, Laser energy-dependent processability of non-equiatomic TiNbMoTaW high-entropy alloy through in-situ alloying of elemental feedstock powders by laser powder bed fusion, Materialia 38 (2024) 102241, https://doi.org/10.1016/j.mtla.2024.102241.
[36] J. Yang, L.M. Schlenger, M.H. Nasab, S.V. Petegem, F. Marone, R.E. Logé, C. Leinenbach, Experimental quantification of inward Marangoni convection and its impact on keyhole threshold in laser powder bed fusion of stainless steel, Addit. Manuf. 84 (2024) 104092, https://doi.org/10.1016/j.addma.2024.104092.
[37] J. Wang, R. Zhu, Y. Liu, L. Zhang, Understanding melt pool characteristics in laser powder bed fusion: an overview of single- and multi-track melt pools for process optimization, Adv. Powder Mater. 2 (2023) 100137, https://doi.org/10.1016/j.apmate.2023.100137.
[38] M. Niinomi, Y. Liu, M. Nakai, H. Liu, H. Li, Biomedical titanium alloys with Young's moduli close to that of cortical bone, Regen. Biomater. 3 (2016) 173–185, https://doi.org/10.1093/rb/rbw016.
[39] H. Matsumoto, S. Watanabe, S. Hanada, Beta TiNbSn alloys with low Young's modulus and high strength, Mater. Trans. 46 (2005) 1070–1078, https://doi.org/10.2320/matertrans.46.1070.
[40] R. Hermann, H. Hermann, M. Calin, B. Büchner, J. Eckert, Elastic constants of single crystalline β-$Ti_{70}Nb_{30}$, Scr. Mater. 66 (2012) 198–201, https://doi.org/10.1016/j.scriptamat.2011.10.039.
[41] P. Wang, M. Todai, T. Nakano, Beta titanium single crystal with bone-like elastic modulus and large crystallographic elastic anisotropy, J. Alloys Compd. 782 (2019) 667–671, https://doi.org/10.1016/j.jallcom.2018.12.236.
[42] R. Duan, S. Li, B. Cai, W. Zhu, F. Ren, M.M. Attallah, A high strength and low modulus metastable β Ti-12Mo-6Zr-2Fe alloy fabricated by laser powder bed fusion in-situ alloying, Addit. Manuf. 37 (2021) 101708, https://doi.org/10.1016/j.addma.2020.101708.
[43] X. Luo, T. Song, A. Gebert, K. Neufeld, I. Kaban, H. Ma, W. Cai, H. Lu, D. Li, N. Li, Y. Li, C. Yang, Programming crystallographic orientation in additive-manufactured beta-type titanium alloy, Adv. Sci. 10 (2023) 2302884, https://doi.org/10.1002/advs.202302884.
[44] H. Schaal, P. Castany, P. Laheurte, T. Gloriant, Design of a low Young's modulus Ti-Zr-Nb-Sn biocompatible alloy by in situ laser powder bed fusion additive manufacturing process, J. Alloys Compd. 966 (2023) 171539, https://doi.org/10.1016/j.jallcom.2023.171539.
[45] M. Tane, K. Yamori, T. Sekino, T. Mayama, Impact of grain shape on the micromechanics-based extraction of single-crystalline elastic constants from polycrystalline samples with crystallographic texture, Acta Mater. 122 (2017) 236–251, https://doi.org/10.1016/j.actamat.2016.09.040.
[46] M. Abdel-Hady Gepreel, M. Niinomi, Biocompatibility of Ti-alloys for long-term implantation, J. Mech. Behav. Biomed. Mater. 20 (2013) 407–415, https://doi.org/10.1016/j.jmbbm.2012.11.014.
[47] Y. Gao, J. Chen, Y. Gan, X. Liang, H. Chen, D. Zeng, C. Yang, W. Jiang, C. Ma, W. Xiao, Biomedical Ti–Nb–O alloy with high strength and ultra-low Young's modulus, Mater. Res. Lett. 13 (2025) 179–187, https://doi.org/10.1080/21663831.2024.2437402.
[48] S. Hanada, O. Izumi, Correlation of tensile properties, deformation modes, and phase stability in commercial β-phase titanium alloys, Metall. Trans. A 18 (1987) 265–271, https://doi.org/10.1007/BF02825707.
[49] S.A. Mantri, M.S.K.K.Y. Nartu, S. Dasari, A. Sharma, P. Agrawal, R. Salloom, F. Sun, E. Ivanov, K. Cho, B. McWilliams, S.G. Srinivasan, N.B. Dahotre, F. Prima, R. Banerjee, Suppression and reactivation of transformation and twinning induced plasticity in laser powder bed fusion additively manufactured Ti–10V–2Fe–3Al, Addit. Manuf. 48 (2021) 102406, https://doi.org/10.1016/j.addma.2021.102406.
[50] W. Zhang, X. Qi, S. Zhong, K. Wang, S. Zhang, Y. Jiao, A. Li, H. Xu, J. Chen, G. Fang, W. Liu, Laser powder bed fusion of metastable β titanium alloys: enhanced strength and plasticity through simultaneous activation of multiple deformation mechanisms, Addit. Manuf. 93 (2024) 104437, https://doi.org/10.1016/j.addma.2024.104437.
[51] J. Zhang, M. Bermingham, J. Otte, Z. Hou, C.H. Ng, D. Kent, X. Huang, M. Dargusch, Designing against ω phase embrittlement in additively manufactured Ti−13.5Mo metastable β titanium alloy through Sn additions, Addit. Manuf. 97 (2025) 104597, https://doi.org/10.1016/j.addma.2024.104597.
[52] M. Tane, H. Nishiyama, A. Umeda, N.L. Okamoto, K. Inoue, M. Luckabauer, Y. Nagai, T. Sekino, T. Nakano, T. Ichitsubo, Diffusionless isothermal omega transformation in titanium alloys driven by quenched-in compositional fluctuations, Phys. Rev. Mater. 3 (2019) 043604, https://doi.org/10.1103/PhysRevMaterials.3.043604.

[53] C. Wang, C.-N. Sun, T. Chang, X. Liang, N. Ma, P. Wang, Orientation-dependent residual stress governs anisotropic warpage in laser powder bed fusion stainless steel: experimental analysis and predictive modelling, Addit. Manuf. 121 (2026) 105158, https://doi.org/10.1016/j.addma.2026.105158.
[54] U.P. Singh, A. Shukla, S. Swaminathan, G. Phanikumar, Effect of build orientations on residual stress, microstructure, and mechanical properties of additively manufactured Alloy-718 components, J. Manuf. Process. 113 (2024) 1–15, https://doi.org/10.1016/j.jmapro.2024.01.047.
[55] J. Schröder, A. Evans, E. Polatidis, J. Čapek, G. Mohr, I. Serrano-Munoz, G. Bruno, Understanding the impact of texture on the micromechanical anisotropy of laser powder bed fused Inconel 718, J. Mater. Sci. 57 (2022) 15036–15058, https://doi.org/10.1007/s10853-022-07499-9.
[56] H. Liu, M. Niinomi, M. Nakai, K. Cho, H. Fujii, Deformation-induced ω-phase transformation in a β-type titanium alloy during tensile deformation, Scr. Mater. 130 (2017) 27–31, https://doi.org/10.1016/j.scriptamat.2016.10.036.
[57] Y. Yang, P. Castany, E. Bertrand, M. Cornen, J.X. Lin, T. Gloriant, Stress release-induced interfacial twin boundary ω phase formation in a β type Ti-based single crystal displaying stress-induced α″ martensitic transformation, Acta Mater. 149 (2018) 97–107, https://doi.org/10.1016/j.actamat.2018.02.036.
[58] X. Zhao, M. Niinomi, M. Nakai, J. Hieda, Effect of deformation-induced ω phase on the mechanical properties of metastable β-type Ti–V alloys, Mater. Trans. 53 (2012) 1379–1384, https://doi.org/10.2320/matertrans.M2012116.
[59] W. Chen, S. Cao, J.Y. Zhang, Y. Zha, Q.M. Hu, J. Sun, New insights into ω-embrittlement in high misfit metastable β-titanium alloys: mechanically-driven ω-mediated amorphization, Mater. Des. 205 (2021) 109724, https://doi.org/10.1016/j.matdes.2021.109724.
[60] F. Brumbauer, S. Arneitz, N.G.J. Helthuis, P. Brunner, N.L. Okamoto, T. Ichitsubo, C. Sommitsch, W. Sprengel, M. Luckabauer, Biomedical β-titanium alloys from pure metal powders - key role of Sn during additive manufacturing, J. Mater. Res. Technol. 39 (2025) 5582–5596, https://doi.org/10.1016/j.jmrt.2025.10.174.
[61] A. Takase, T. Ishimoto, R. Suganuma, T. Nakano, Surface residual stress and phase stability in unstable β-type Ti–15Mo–5Zr–3Al alloy manufactured by laser and electron beam powder bed fusion technologies, Addit. Manuf. 47 (2021) 102257, https://doi.org/10.1016/j.addma.2021.102257.
[62] S. Goel, M. Neikter, J. Capek, E. Polatidis, M.H. Colliander, S. Joshi, R. Pederson, Residual stress determination by neutron diffraction in powder bed fusion-built Alloy 718: influence of process parameters and post-treatment, Mater. Des. 195 (2020) 109045, https://doi.org/10.1016/j.matdes.2020.109045.
[63] S.H. Sun, K. Hagihara, T. Ishimoto, R. Suganuma, Y.F. Xue, T. Nakano, Comparison of microstructure, crystallographic texture, and mechanical properties in Ti–15Mo–5Zr–3Al alloys fabricated via electron and laser beam powder bed fusion technologies, Addit. Manuf. 47 (2021) 102329, https://doi.org/10.1016/j.addma.2021.102329.
[64] K. Cho, K. Yamashita, S. Kakutani, T. Saito, T. Sasaki, K. Sawaizumi, O. Gokcekaya, T. Ishimoto, H. Kimizuka, W. Gong, T. Kawasaki, S. Harjo, T. Nakano, H.Y. Yasuda, Effect of nanoscale cellular structure on the mechanical properties of Inconel 718 with unique hierarchical structure fabricated by laser powder bed fusion, Acta Mater. 303 (2026) 121696, https://doi.org/10.1016/j.actamat.2025.121696.
[65] X. Li, R. Esmaeilizadeh, E. Hosseini, Microstructure and mechanical response of as-built and solution-annealed LPBF Hastelloy X under high-temperature fatigue loading, Addit. Manuf. Lett. 10 (2024) 100227, https://doi.org/10.1016/j.addlet.2024.100227.
[66] Y. Tsutsumi, T. Ishimoto, T. Oishi, T. Manaka, P. Chen, M. Ashida, K. Doi, H. Katayama, T. Hanawa, T. Nakano, Crystallographic texture- and grain boundary density-independent improvement of corrosion resistance in austenitic 316L stainless steel fabricated via laser powder bed fusion, Addit. Manuf. 45 (2021) 102066, https://doi.org/10.1016/j.addma.2021.102066.
[67] M.S. Pham, B. Dovgyy, P.A. Hooper, C.M. Gourlay, A. Piglione, The role of side-branching in microstructure development in laser powder-bed fusion, Nat. Comm. 11 (2020) 749, https://doi.org/10.1038/s41467-020-14453-3.
[68] H. Chen, D. Egusa, Z. Li, T. Sasaki, R. Ozasa, T. Ishimoto, M. Okugawa, Y. Koizumi, T. Nakano, E. Abe, Phase-separation induced dislocation-network cellular structures in Ti-Zr-Nb-Mo-Ta high-entropy alloy processed by laser powder bed fusion, Addit. Manuf. 102 (2025) 104737, https://doi.org/10.1016/j.addma.2025.104737.
[69] T. Kikukawa, T. Ishimoto, H.S. Kim, T. Nakano, Remarkable strengthening effects of cells in laser powder bed fusion-processed Inconel 718, Mater. Res. Lett. 13 (2025) 837–843, https://doi.org/10.1080/21663831.2025.2522801.
[70] C. Wei, L. Li, Recent progress and scientific challenges in multi-material additive manufacturing via laser-based powder bed fusion, Virtual Phys. Prototyp. 16 (2021) 347–371, https://doi.org/10.1080/17452759.2021.1928520.
[71] X. Li, T. Saario, T. Ikäläinen, Z. Que, Corrosion behavior of additively manufactured M300-CuCr1Zr by multi-material laser-based powder bed fusion, Electrochim. Acta 507 (2024) 145199, https://doi.org/10.1016/j.electacta.2024.145199.